PAPER

Momentum Distribution in the Wake of a Trapezoidal Pitching Panel

AUTHORS

Rajeev Kumar
Justin T. King
Melissa A. Green
Department of Mechanical and Aerospace Engineering, Syracuse University

ABSTRACT

The oscillation of bioinspired fin-like panels in a uniform freestream flow creates chains of vortex rings, including streamwise segments that induce significant three-dimensional effects. With increasing Strouhal number, this wake structure induces flow with increasing nondimensional momentum, defined relative to the freestream velocity, in the downstream direction. This increase in relative momentum with increasing Strouhal number is consistent with greater nondimensional thrust production, which has been shown previously in the literature. These results were obtained via stereoscopic particle image velocimetry water tunnel experiments at Strouhal numbers ranging from 0.17 to 0.56 downstream of a continuously pitching trapezoidal panel. Features of the wake dynamics including spanwise compression, transverse expansion, transverse wake splitting or bifurcation, and wake breakdown are elucidated through analyses of phase-averaged as well as time-averaged velocity fields, in addition to common vortex identification methods.

Keywords: stereoscopic PIV, trapezoidal pitching panel, Strouhal number, wake vortex structure, bioinspired propulsion

Introduction

A majority of marine animals propel themselves by transferring momentum to the surrounding fluid by oscillating their fins and flukes. There is a paucity of high aspect ratio ($AR = b^2/S$, where b is the span and S is the planform area) fins in marine animals in contrast to relative abundance of high AR wings in flying animals, which is largely due to water being almost a thousand times denser than air. The flapping and pitching of high AR fins would face large resistance due to added mass effects of water (Dong et al., 2006). Marine animals have therefore evolved with low AR fins and have adapted to performance degradation associated with inevitable three-dimensional (3D) effects. Highly 3D wakes are far more complex than the two-dimensional (2D) wakes contemplated in many theoretical models. Many previously studied 2D wakes behind oscillating bluff bodies, airfoils, and plates are characterized by two single counter-rotating spanwise-oriented vortices shed at the trailing edge during each pitching cycle, resulting in a vortex street formation referred to as 2S (Williamson & Roshko, 1988). If these counter-rotating vortices are aligned such that the vortex-induced velocity is oriented downstream, the formation can also be referred to as a reverse von Karman vortex street (Triantafyllou et al., 2000; Koochesfahani, 1989; Anderson et al., 1998). The transition of a 2D wake from the classical von Karman vortex street to a reverse von Karman vortex street can occur with increasing Strouhal number, $St = fA/U$, where f is the fin/foil flapping frequency, A is the wake width usually approximated by the trailing edge peak-to-peak amplitude, and U is the freestream velocity. This transition has been shown to precede net thrust generation (Godoy-Diana et al., 2008; von Ellenrieder & Pothos, 2008) and was found to occur at St = 0.12 and 0.31, respectively, in an experimental and numerical investigation on a NACA-0012 foil pitched at an amplitude of ±5° (Yu et al., 2012).

These 2D flows past oscillating foils are mainly governed by Strouhal number, while Reynolds number ($Re = cU/\nu$, where c is the chord of the oscillating body and ν is the kinematic viscosity of the fluid) plays a minor role as long as Re is $O(1000)$ or greater (Triantafyllou, Triantafyllou, & Grosenbaugh, 1993). For low AR fins and foils, changing AR itself will also have significant effects on thrust, efficiency, and wake structure (von Ellenrieder et al., 2003; Ghovardhan & Williamson, 2005; Guglielmini, 2004; Dong et al., 2006; Zhu & Shoele, 2008; Green & Smits, 2008). 3D wakes of low AR propulsors have been shown to transition from 2S type to 2P type with increasing St or decreasing AR by Buchholz and Smits (2006) in experiments. In 2P wakes, two pairs of oppositely signed vortices are shed during each pitching cycle such that the induced velocity from each pair effectively splits the wake into two, a phenomenon also observed in the wake of an undulatory swimmer by Hultmark et al. (2007). In some previous results, the structure of the wake downstream of the trailing edge of bioinspired pitching panels was inferred to be established by the distribution of vorticity on the panel surface before the vortices were shed (Buchholz & Smits, 2008; Buchholz, Green, & Smits, 2011). These wakes transition from 2S to 2P configuration at a *St* very close to the range of $0.25 < St < 0.35$, in which real fish have been observed to swim with optimal propulsive efficiency (Triantafyllou et al., 1993). This range was also predicted using linear stability analysis on an oscillatory foil and subsequently confirmed by the findings of 2D flapping foil experiments. An understanding of the phenomenon of wake transition from 2S to 2P and the transition process between those two states will be integral to the physical description of optimal swimming and the design of an optimal bioinspired propulsor.

Buchholz and Smits (2008) and Clark and Smits (2006) reported peak propulsive efficiency occurring in range $0.1 < St < 0.3$ in their experiments on a rigid rectangular pitching panel and on a batoid-inspired flexible fin, respectively. For the rectangular plate, the peak efficiency occurred at $St = 0.21$ and transition from 2S to 2P occurred at $St = 0.41$, whereas for the batoid-inspired flexible fin, peak efficiency occurred at $St = 0.25$ and the transition at $St = 0.3$. These observations from two different models showed that fin flexibility, in addition to geometry, may also play a role in the transition to a 2P type wake. Dewey et al. (2012) extended the work on batoid-inspired flexible fins by Clark and Smits (2006) with a focus on studying the effect of flexible body wavelength and Strouhal number on the 3D wake structure that relate to propulsion and efficiency. They found that efficiency is maximized when a 2S wake structure is present at the midspan of the fin that does not transversely split or bifurcate within one chord length downstream of the fin. They also found a bifurcated wake to be less efficient. It is also interesting to note that, in these previous results, wake bifurcation was not associated with drastic or discontinuous loss of efficiency.

3D effects are introduced into the wake of an oscillating fin through the tip vortices that combine with the spanwise-oriented vortices generated by the motion of the trailing edge to form a system of horseshoe vortex structures. Parker et al. (2005, 2007a, 2007b) analyzed the organization and evolution of the wake structures downstream of low *AR* foils using digital particle image velocimetry (PIV). von Ellenrieder et al. (2003) captured these structures on a rectangular ($AR = 3$) flapping foil at $Re = 164$, $0.2 < St < 0.35$, and pitch angle amplitudes up to 20° using dye flow visualization. This work was numerically studied by Guglielmini and Blondeaux (2004) and Blondeaux et al. (2005b), where they found increased interaction among the adjacent vortex loops with increasing *St*. The wake was dominated by the continuously shed horseshoe vortex systems that evolve into an intricate chain of vortex rings while convecting downstream (Buchholz & Smits, 2006). Other 3D effects, such as spanwise wake compression and transverse expansion have been observed to take place due to these interactions as well.

Drucker and Lauder (1999) reconstructed the vortex field downstream of bluegill sunfish pectoral fins by quantifying velocity fields in three perpendicular planes recorded using digital PIV. Vorticity shed by each fin during the downstroke and stroke reversal generated discrete vortex rings of near-uniform circulation. Shed vortex rings induce their own local flow fields and in certain patterns can increase downstream momentum, indicative of thrust generation. This implies that thrust vectoring could potentially be achieved by changing the kinematics and gait of the fins (Drucker & Lauder, 2002). Dong et al. (2006) used numerical simulation to generate detailed wake topologies and computed hydrodynamic forces on thin ellipsoidal flapping foils modeling fish pectoral fins for a range of Strouhal and Reynolds numbers. The magnitude and organization of momentum transfer between the marine animal and the surrounding fluid is inferred to be critical to understanding the fundamental physical mechanism governing fish swimming (Dabiri, 2005; Epps & Techet, 2007).

Two sets of interconnected vortex loops (vortex rings in lower *AR* fins; Drucker & Lauder, 2002) are important 3D effects due to their central role in momentum generation and distribution in the wake. Researchers mentioned above carried out experimental and numerical studies on finite *AR* oscillating fins and foils to capture the wake structures. A few of them also analyzed velocity fields in the midspan plane. A majority of these studies are aimed at visualization using PIV with analysis of phase-averaged and time-averaged velocity fields only in 2D wake planes. Few, however, analyzed 3D velocity fields caused by the wake structures that would shed light into the wake behavior.

Spanwise coherent structures behind an oscillating trapezoidal panel modeling a caudal fin were studied by Green et al. (2011) using finite-time Lyapunov exponents (FTLE), a Lagrangian analysis technique. 2D velocity fields at each plane were captured using PIV, but in the absence of the out of plane velocity, streamwise and transverse vorticity fields were not computed and only FTLE results at the midspan were considered.

In the current study, further insight into the wake dynamics of a caudal fin, modeled as a trapezoidal pitching panel, has been obtained via the 3D field analysis that focuses on the velocity fields. The wake downstream of the panel is captured using stereoscopic PIV, and the wake vortex structures are visualized by plotting isosurfaces of Q-criterion. The 3D organization of momentum in the wake of this finite AR fin, which distinguishes it from 2D wakes, is studied by analyzing both phase-averaged and time-averaged velocity fields as a function of St. Observed 3D effects include the formation of two sets of interconnected vortex loops that induce downstream momentum and result in momentum-rich splitting or bifurcating jets and trapped sluggish fluid regions. The spatial distribution of these features possibly explains the trade-off between thrust and efficiency at higher St.

Experimental Setup

The experiments were carried out in a recirculating water tunnel having rectangular test section (0.60 m × 0.60 m × 2.44 m) located at the Syracuse University Center of Excellence. The water surface of the test section was enclosed by a large acrylic cover in order to minimize surface effects. A honeycomb flow straightener and three screens were installed upstream of the test section to condition the flow. An average turbulence intensity of roughly 6% was recorded at the highest Reynolds number tested. Two Nikon HiSenseMKI CCD cameras, operated with a resolution of 1,280 × 1,024 pixels, were mounted at an angle to each other placed above the test section. The cameras were aligned in an angular displacement stereoscopic PIV arrangement, allowing for all three components of velocity to be measured. A New Wave Gemini 200-15 Nd-YAG pulsed laser was used to illuminate the flow in a plane at a desired location along the span of the panel. A schematic of the test section, laser, and camera setup can be seen in Figure 1. The positive x-axis is directed along the freestream, the y-axis lies along the transverse direction, and the z-axis is oriented in the spanwise direction as shown in the figure.

The trapezoidal planform chosen for the panel approximately models the shape of a fish caudal fin. The 1.59-mm-thick panel had sharp (unrounded) edges and was made out of rigid acrylic. The trailing edge span was 254 mm, the chord length was 101 mm, and the length of the leading edge was 52 mm resulting in an $AR \approx 4.17$. For the trapezoidal panel, aspect ratio is calculated as $AR = b^2/S$, where b is the span of the trailing edge and S is the planform area per usual. The angle created by the swept edges of the panel was 45°, and the panel was pitched around its leading edge through an angle of ±7.5°, measured from in-line with the freestream flow. A schematic of the panel with detailed dimensions is shown in Figure 1b.

The panel was attached at its leading edge to a circular pitching shaft of 4.76-mm diameter. The panel and pitching shaft were mounted downstream of and in-line with a NACA-0012 fairing. The trailing edge of the fairing was truncated, making room for the shaft and giving the fairing a chord length of 50.8 mm. A series 38A Faulhaber DC micromotor with a 20:1 gear ratio powered the shaft and the motor was controlled by a Galil DMC-4123 four axis motion controller. The angular position of the shaft was monitored with an

FIGURE 1

Schematic of experimental setup, trapezoidal panel specifications, and data planes and the volume of interpolation.

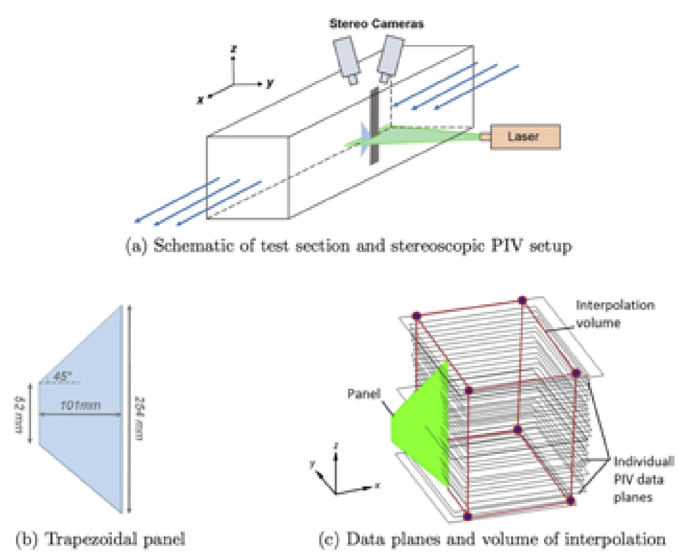

Avago HEDS-5500 optical encoder having a resolution of 1,024 counts per revolution.

The laser and two cameras were mounted on a traverse assembly; therefore, the physical distance between the cameras and the laser sheet remained constant for all planes of collected data. PIV images were collected at 29 different planes across the span of the panel. The planes were spaced 10 mm apart, except for the planes at the top, bottom, and middle, which were 2 mm, 2 mm, and 5 mm, respectively, from the neighboring planes. The traverse assembly allowed for controlled movement of cameras and the laser among the studied spanwise locations. A Dantec linear traverse that was controlled by an Isel C142-4 controller box was used. A schematic of the traverse assembly that displays the laser and two cameras is shown in Figure 2.

Cameras were calibrated in each of the 29 data planes across the span with a dotted, two-level stereoscopic PIV calibration target using a pinhole camera model. Across all data planes, the calibrations had an average reprojection error of 0.25. The accuracy of the imaging model fit used for a stereoscopic calibration is considered to be acceptable when the reprojection error is below 0.5 (Martínez-Suástegui, 2012). Dantec Dynamics polyamide seeding particles with a diameter of roughly 20 μm were used. The analysis and collection of PIV images in each data plane were carried out with Dantec DynamicStudio v3.31 software. Images were evaluated with an adaptive correlation method for an interrogation window of 16 × 16 pixels with 50% overlap in the horizontal and vertical directions. All analysis began with an initial interrogation area window size of 64 × 64 pixels, and two refinement steps were used. Particle image diameters were calculated to be approximately 1.2 pixels. For this particle image diameter, Monte Carlo simulations show that the RMS random error for cross-correlation digital PIV using a 16 × 16 pixel interrogation window is approximately 0.07 pixels (Raffel et al., 2007).

A BNC 575 programmable power supply was used to coordinate and control the timing of the cameras and laser. The cameras and laser were synchronized and operated at a rate of 4 Hz. Images were recorded and analyzed over 19 periods at 24 unique phases in the pitching cycle, and phase-averaged velocity data were obtained from these images. Five pairs of Strouhal and Reynolds numbers were obtained by manipulating the freestream velocity of the water tunnel while holding pitching frequency and pitching amplitude constant across runs as presented in Table 1.

FIGURE 2

Linear traverse assembly with lasers and overhead cameras.

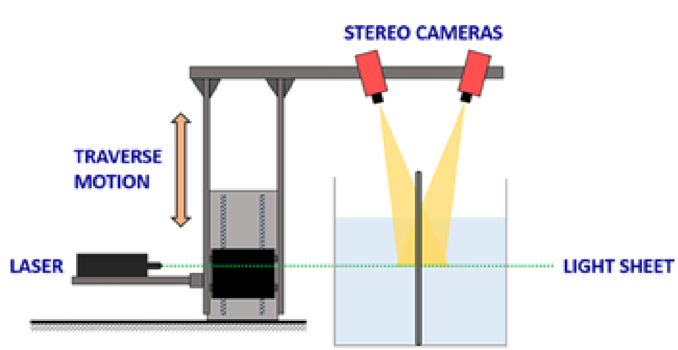

TABLE 1

Summary of experimental parameters.

St	*U*, mm/s	*Re* ($\times 10^3$)
0.17	156	15.9
0.27	99	10.2
0.37	73	7.4
0.46	57	5.8
0.56	47	4.8

Results

The phase-averaged velocity data from the original 29 planes were interpolated into a common volume intersecting all the planes (see Figure 1c). The interpolation was carried out employing a cubic spline function in MATLAB. A spatial resolution of approximately 2 mm × 2 mm × 2.5 mm was obtained in the x, y, and z directions, respectively, which was fine enough to resolve the spatial gradients of velocity field. It is important to note that any flow pattern or structure that is smaller than this grid spacing (0.025c) will not be captured from this data interpolation.

The vorticity and the Q-criterion fields were computed using the phase-averaged velocity field, which in nondimensional form is expressed as:

$$\langle \mathbf{u} \rangle = \langle u', v', w' \rangle / U \tag{1}$$

where $\langle\ '\rangle$ denotes a phase-averaged dimensional variable and U is the freestream velocity. The Q-criterion is an Eulerian analysis tool that is useful for vortex identification and is calculated from the Euclidean or Frobenius norms of both the rate-of-rotation tensor and the rate-of-strain tensor as defined as,

$$\boldsymbol{Q} = \frac{1}{2}\left[||\boldsymbol{\Omega}||^2 - ||\boldsymbol{S}||^2\right] \quad (2)$$

where $\boldsymbol{\Omega}$ is the antisymmetric rate of rotation tensor and $\boldsymbol{S}$ is the symmetric rate of strain tensor, both found from the standard decomposition of the velocity gradient (Hunt, Wray, & Moin, 1988). According to the Q-criterion definition, a vortex exists in regions where $Q > 0$; i.e., in a region where the rate-of-rotation tensor dominates the rate-of-strain tensor. In all figures that follow, vortex structures are visualized as isosurfaces of Q at 1% of the maximum value over the whole pitching period across all *St*.

3D effects enter into the wake behind an oscillating panel or fin as streamwise vortices roll up at the tips and form the legs of a horseshoe vortex system released at the trailing edge and giving rise to a vortex-ring-dominated wake structure. This structure creates two sets of interconnected vortex loops that connect and overlap as they convect downstream. They also induce flow through the ring portions and can create jet-like streams that diverge in the transverse (y) direction. The overall wake topology and behavior displaying these phenomena and the multiple jet-like streams are represented by isosurfaces of phase-averaged and time-averaged streamwise components of the velocity field, paired with phase-averaged Q isosurfaces to show the orientation of the vortex structures.

The nondimensional time-averaged velocity field $\overline{\mathbf{u}}$ (x, y, z) was calculated by averaging the nondimensional phase-averaged velocity field over a cycle comprising of the 24 sets of phase-averaged data such that,

$$\overline{\mathbf{u}}(x,y,z) = \frac{1}{24}\sum_{t/T=0}^{23}\left\langle u,v,w\right\rangle_{t/T} \quad (3)$$

Perspective views of the wake structures, isosurfaces of the phase-averaged streamwise velocity, and isosurfaces of the time-averaged streamwise velocity have been presented for all five Strouhal numbers in Figure 3. Here, the data are presented at the phase $t/T = 0$, where the panel trailing edge is currently aligned with the freestream and moving to the right, as seen from downstream in the figure. The left column visualizes wake structures as isosurfaces of positive Q. In Figure 3 and subsequently, isosurfaces of 1% of the

FIGURE 3

Visualization of overall wake structure at $t/T = 0$ for all five Strouhal numbers. Left column: isosurfaces of 1% Q_{max} colored by the spanwise vorticity (ω_z). Middle column: isosurfaces of 1% Q_{max} colored (gray) and isosurfaces of phase-averaged streamwise velocity ($\langle u \rangle$). Right column: isosurfaces of time-averaged streamwise velocity, $\overline{u}$. (Color versions of figures are available online at http://www.ingentaconnect.com/content/mts/mtsj/2016/00000050/00000005.)

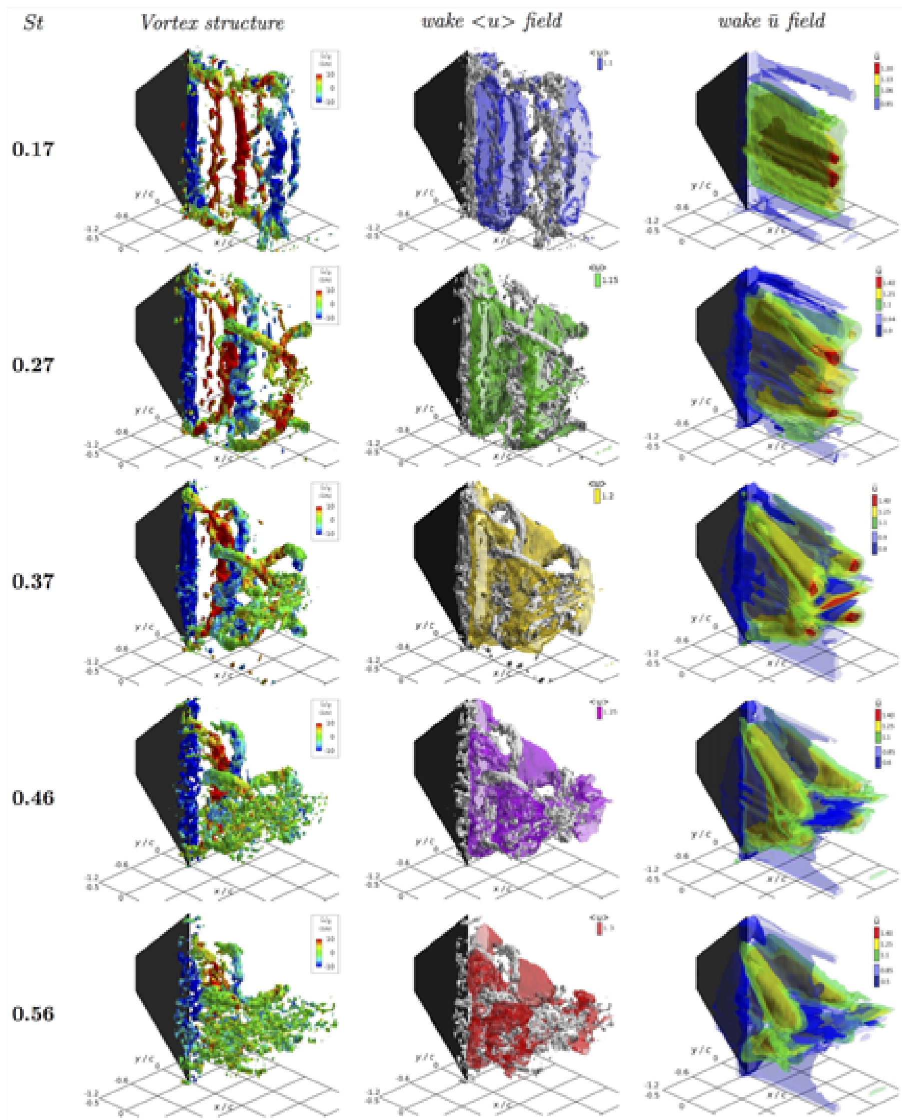

maximum value of Q are used for vortex wake visualization. In the left column, the surfaces are color-coded from blue to red by the spanwise vorticity, ω_z. Isosurfaces of nondimensional phase-averaged streamwise velocity $\langle u \rangle$ are shown in the middle column superimposed on Q isosurfaces (gray). The vortex ring structures induce accelerated flow through their center as indicated by the colored isosurfaces of phase averaged streamwise velocity $\langle u \rangle > 1$. The right column of figures presents the isosurfaces of nondimensional time-averaged streamwise velocity, $\overline{u}$, in the wake at four or five isosurface levels.

During each half-period of motion, the pitching panel creates and releases a horseshoe vortex, generated by vorticity rolling up at the trailing edge (shaded red or blue in the left column in Figure 3), and quasi-streamwise-oriented vortices that roll up at both diagonal edges.

At the phase presented in Figure 3, the spanwise vorticity of the structure being formed as the trailing edge moves to the right is negative, and hence, the isosurface is shaded blue. As a new horseshoe vortex is formed in subsequent half-periods, the streamwise segments of neighboring vortex loops interact and twist around each other, forming the vortex chain commonly seen in similar wakes generated by unsteady bioinspired aerodynamic and hydrodynamic surfaces. As St increases, the streamwise vortices also move in the transverse (cross-wake) direction while convecting downstream, which causes a bending of the coherent structures depending on the rotation of each subsequent loop. This results in an observed spanwise compression and transverse expansion. At higher St, the spanwise structures can also lose coherence and disintegrate downstream, a phenomenon that has been referred to as wake breakdown (Green et al., 2011). This phenomenon occurs farther upstream with increasing St.

In the middle column of Figure 3, isosurfaces of phase-averaged velocity were plotted at increasing levels for the five different Strouhal numbers. This is to elucidate that higher momentum relative to the freestream flow is observed with increasing St, but the spatial structure of high-momentum fluid is consistently associated with the center of each vortex loop. At $St = 0.17$ (top row of Figure 3, middle column), the blue isosurfaces indicate fluid that has a streamwise velocity 10% higher than the freestream. A similar region is shown in yellow for $St = 0.37$ (third row), but in this case, the streamwise velocity isosurface is 20% higher than freestream. At the highest Strouhal number, $St = 0.56$ (bottom row), the similarly organized streamwise velocity isosurface, here shown in red, is at 30% higher than the freestream velocity. It is important to note that while the percentage momentum gain increases with St, the freestream momentum also decreases (decreasing U for increasing St).

Isosurfaces for the time-averaged velocity $\overline{u}$ have been plotted in the right column of Figure 3 to indicate regions of $\overline{u} > 1$ (green, yellow, and red) and $\overline{u} < 1$ (blue). The wake's high-momentum core transforms from a predominantly rectangular shaped cross-section at $St = 0.17$, to an organization with multiple high momentum cores and a deformed shape that is consistent with the spanwise compression and transverse expansion of the wake with increasing St. The overall topology and behavior of the wake downstream of the pitching panel have been analyzed in more detail with the help of phase-averaged and time-averaged velocity isosurfaces at three representative St.

Phase-Averaged Velocity Fields

Lowest Strouhal Number:* St = *0.17

In Figures 4a, 4b, and 4c, isosurfaces of phase-averaged streamwise velocity are superimposed with the wake vortex structures at $St = 0.17$ and phase $t/T = 0.25$. The panel at $t/T = 0.25$ is at the end of the upstroke and just about to begin its downstroke as seen from above. The flow induced and accelerated by the vortex structures is outlined by a blue isosurface at a level of $\langle u \rangle = 1.1$. Spanwise compression and vortex breakdown are not apparent at this lowest St, possibly due to the large streamwise spacing, and therefore decreased interaction, between vortex loops. Spanwise compression is caused by mutual induction of the streamwise counter rotating pairs of overlapping consecutive horseshoes (Buchholz & Smits, 2006).

It is clear, particularly when viewed from above in Figure 4c, that the accelerated streamwise flow is associated with regions where the vortex-loop-induced velocity is oriented downstream in accordance with the right-hand rule. To show this more clearly, the phase-averaged velocity vectors in the midspan ($z = 0$) plane with contours of ω_z in the background are shown in Figure 4d. Because this plane is at the midspan, the spanwise flow (into and out of the page) is small relative to the streamwise and transverse flow, so the velocity vectors stay mostly in the plane. The region of $\langle u \rangle$ greater than 1.1 near $x/c \approx 1.5$, between $-0.6 < y/c < 0$ seen from the top view (Figure 4c) is associated with the vortex loop that can be seen in the cross section of Figure 4d that includes the positive (red) spanwise vortex tube at $x/c = 1.5$ and the negative (blue) spanwise

FIGURE 4

Visualization of overall wake structure at $t/T = 0.25$ for $St = 0.17$. Panels a–c show isosurfaces of 1% Q_{max} colored in gray. Panels a–c also show the isosurfaces of $\langle u \rangle = 1.1$. Panel 4d displays the distribution of ω_z at the midspan plane in the background of the phase-averaged streamwise velocity vector field.

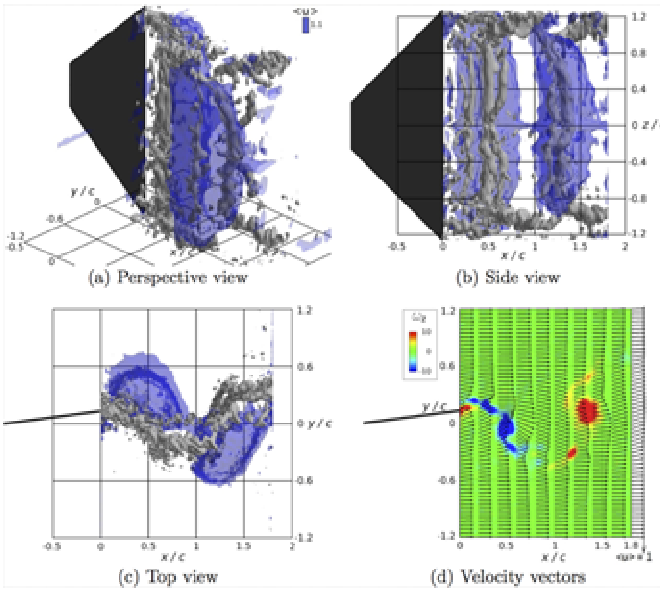

vortex tube near $x/c = 0.5$. In addition, the increased momentum in this wake is observed from the velocity vectors at the midspan by the fact that a portion of the vectors at the downstream exit plane slightly exceed $\langle u \rangle = 1$ at this phase, which is indicated by a solid vertical line to the right of Figure 4d. This effect is more pronounced in the time-averaged results, as will be shown in the Lowest Strouhal Number subsection of the Time-Averaged Velocity Fields section.

Intermediate Strouhal Number: St = *0.37*

In Figures 5a, 5b, and 5c, isosurfaces of phase-averaged streamwise velocity are superimposed with the wake vortex structures at $St = 0.37$ and phase $t/T = 0.25$ when the panel is just about to begin its downstroke as viewed from above. Yellow isosurfaces are shown at $\langle u \rangle = 1.2$ at this Strouhal number but cover the entire region between vortex loops, implying that the vortex structure induces higher momentum relative to the freestream as the St increases. Discernible spanwise compression and transverse expansion of the wake are also observed at this St. The spanwise vortices are more closely spaced, as seen clearly from the side (Figure 5b), resulting in increased interaction between consecutive streamwise vortex structures, evident in Figure 5c (Buchholz & Smits, 2006; Green et al., 2011). Overlapping of vortex structures also results in vortex loop bending and eventual disintegration of the coherent structures in wake breakdown.

Figure 5d shows the phase-averaged velocity vectors at the midspan with contours of ω_z in the background, and it is clear that the spanwise vortex tubes start to lose coherence by 1.25 chord lengths downstream where they begin to break apart and lose vorticity

FIGURE 5

Visualization of overall wake structure at $t/T = 0.25$ for $St = 0.37$. Panels a–c show isosurfaces of 1% Q_{max} colored in gray. Panels a–c also show the isosurfaces of $\langle u \rangle = 1.2$. Panel 5 displays the distribution of ω_z at the midspan plane in the background of the phase-averaged streamwise velocity vector field.

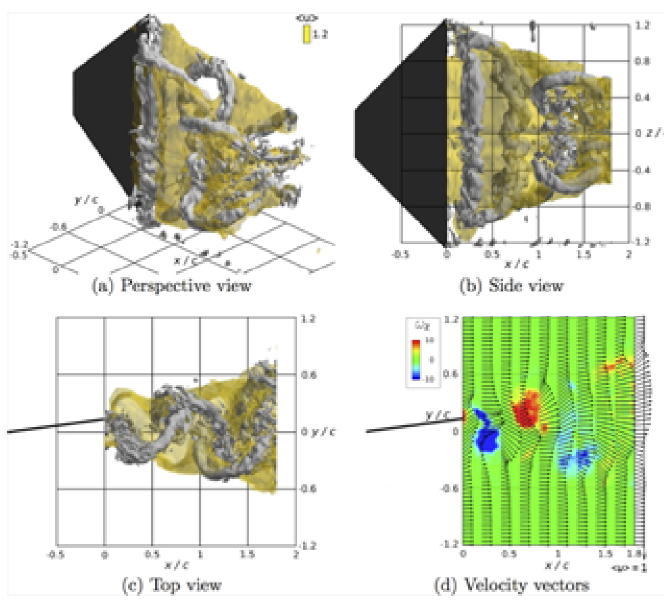

magnitude. At this *St*, the interconnected vortex loops also begin to diverge and induce flow away from the wake centerline in the transverse (y) direction. This too is consistent with the direction of velocity vectors at the downstream exit plane near $y/c \pm 0.6$.

Highest Strouhal Number:* St = *0.56

In Figures 6a, 6b, and 6c, isosurfaces of phase-averaged streamwise velocity are superimposed with the wake vortex structures at $St = 0.56$ and phase $t/T = 0.25$. Red isosurfaces are shown at $\langle u \rangle = 1.3$ at this *St* because vortex structures at increased *St* continue to induce higher momentum relative to the freestream. The divergence of two sets of interconnected less coherent vortex loops is now clearly observed from the top view (Figure 6c) with the emergence of a *V*-shaped pair of jets. A zone of sluggish recirculating fluid is created between these two diverging jets, near $y/c = 0$, downstream of $x/c = 1$. The phenomena of spanwise compression, transverse expansion, and wake breakdown are most pronounced at this highest *St*, consistent with decreased distance between consecutive vortex loops and increased vortex loop interaction. Phase-averaged vorticity (ω_z) contours and velocity vectors in the spanwise symmetry plane in Figure 6d also confirm this, as coherent spanwise vortices are only observed upstream of $x/c = 0.75$. The exit velocity vector profile shows widespread low-momentum fluid distributed asymmetrically on either side of the $y/c = 0$ axis downstream of sluggish region between the jets. This low-momentum stretch however is enclosed by two smaller high-momentum regions near $y/c \approx -0.5$ and ≈ 1 at the downstream exit plane at this phase, representing the two jets produced by the diverging jets.

FIGURE 6

Visualization of overall wake structure at $t/T = 0.25$ for $St = 0.56$. Panels a–c show isosurfaces of 1% Q_{max} colored in *gray*. Panels a–c also show the isosurfaces of $\langle u \rangle = 1.3$. Panel d displays the distribution of ω_z at the midspan plane in the background of the phase-averaged streamwise velocity vector field.

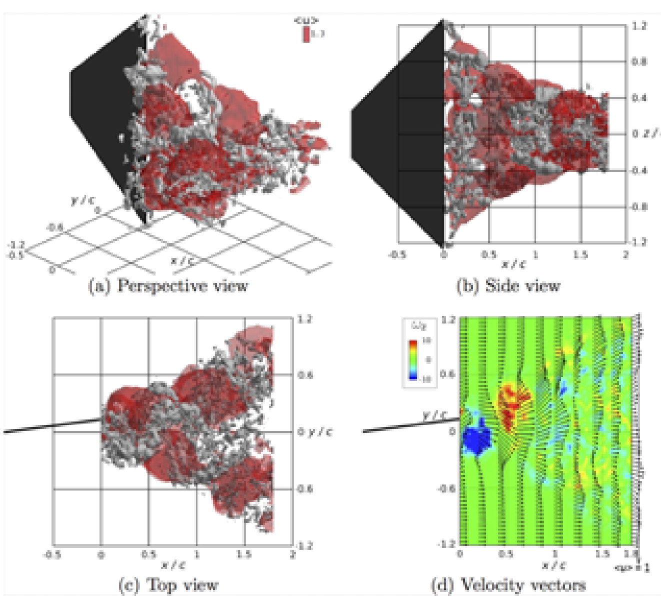

Time-Averaged Velocity Fields

Time-averaged velocity fields provide insight into overall wake topology and wake behavior in the average sense. The wake topology and behavior at the same three representative *St* cases are presented by plotting the isosurfaces of the streamwise component of nondimensional time-averaged velocity ($\overline{u}$) field. The isosurfaces with $\overline{u} > 1$ encapsulate flow with momentum in excess of the freestream and $\overline{u} < 1$ indicates flow with a momentum-deficit compared to freestream.

Lowest Strouhal Number:* St = *0.17

Four views of time-averaged streamwise velocity ($\overline{u}$) isosurfaces are shown for the lowest Strouhal number studied ($St = 0.17$) in Figure 7. Isosurfaces have been plotted at $\overline{u} = 1.06$ (green), 1.13 (yellow), and 1.2 (red) to capture the momentum surplus region of the wake. One isosurface at $\overline{u} = 0.95$ (blue) captures the momentum deficit regions.

The time-averaged wake consists of a momentum-rich core along the centerline of the wake between two momentum-deficient regions that appear as two long antennae-like tubular regions downstream of the panel's spanwise tips, which diverge in the transverse direction. The velocity increases toward the center of the wake with the zone of highest momentum around the midspan region where the flow is quasi-2D. The momentum-surplus wake stretches across almost two thirds of the span while momentum-deficient wake covers around one third of the span near the tips. Green et al. (2011), in their experiments on a similar trapezoidal panel oscillating at $St = 0.17$ and 0.28, observed that the vortices in the midspan region arrange in a clear 2S thrust-producing pattern with induced jet directed

FIGURE 7

Visualization of the overall wake structure in terms of the time-averaged streamwise velocity for $St = 0.17$. Panels a–d present isosurfaces of $\overline{u}$ that range from 0.95 to 1.20. Panel e shows the distribution of velocity vectors and contours at the plane of the midspan. Panels f–h show the spanwise distribution of $\overline{u}$ at three streamwise locations.

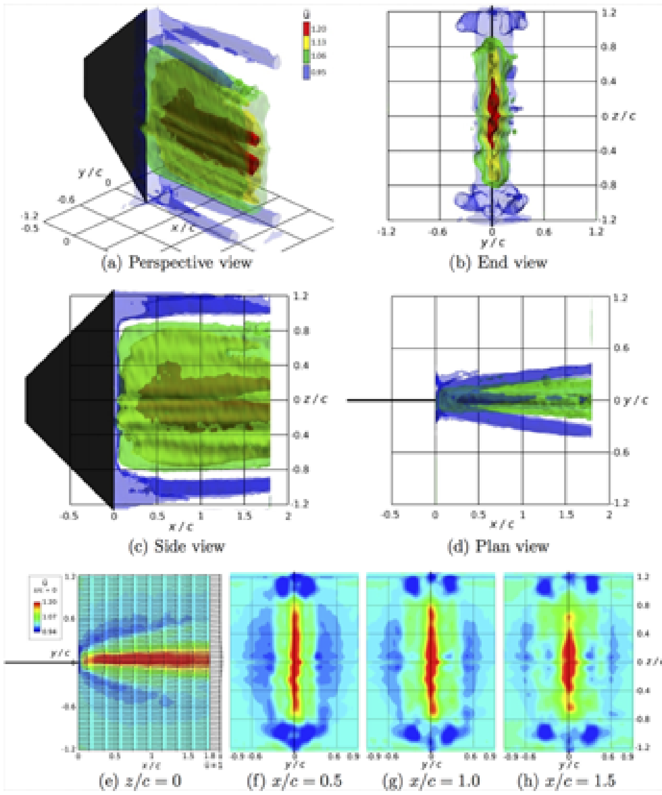

downstream. Interestingly, near the panel tip, the vortices formed a 2S pattern with induced jet directed upstream, indicating a reduction in streamwise momentum, consistent with the findings in present study.

The shape of the time-averaged wake is largely rectangular both in profile as well as cross-section, which indicates the near-absence of spanwise wake compression and transverse expansion within the data domain. This is also supported by the time-averaged streamwise velocity contours and vectors in the spanwise symmetry plane and contours in three different streamwise planes at $x/c = 0.5$, 1.0, and 1.5 in Figures 7e–7h. The high-momentum jet in the middle does not widen significantly, and the velocity vectors appear largely parallel with the streamwise direction in this view, consistent with the relatively small amount of transverse wake expansion. The velocity vector profile at the exit has a low-magnitude bump near $y/c = 0$ where arrows cross a $\overline{u} = 1.0$ line, indicating the momentum surplus in the region. The time-averaged streamwise velocity contour plots at three downstream locations show a high-momentum core toward the center that contracts in height as the contour plane moves to downstream locations.

Also visible are the streamwise-oriented momentum-deficient tubes that emanate from the spanwise panel tips. These tubes are mostly horizontal but do exhibit outward transverse displacement, most clearly seen from above (Figure 7d) or in the cross stream planes (Figures 7f–7h). By comparing Figure 7d with Figure 4c, it is clear that these regions of decreased streamwise momentum are in the same spatial location as the top edges of the vortex loops (e.g., in the top half of the wake, $z/c \approx 1$, $y/c \approx \pm 0.4$ at the edge of the data domain).

Intermediate Strouhal Number: St = *0.37*

Four views of time-averaged streamwise velocity ($\overline{u}$) isosurfaces are shown for the middle Strouhal number studied ($St = 0.37$) in Figure 8. Isosurfaces have been plotted at $\overline{u} = 1.1$ (green), 1.25 (yellow), and 1.4 (red) to capture the momentum-surplus regions of the wake. Two isosurfaces at $\overline{u} = 0.8$ and 0.95 (dark blue, light blue) capture the momentum-deficit regions.

Significant spanwise compression and transverse expansion of the time-averaged wake can be observed at this *St*. Higher-momentum regions behind the trailing edge stretch between $z/c = \pm 0.8$ at one chord length downstream ($x/c = 1$) and across $z/c = \pm 0.5$ by the end of the data window. As observed in the phase-averaged velocity results, the jets formed by the interconnected vortex loops diverge away from the centerline. What was not clear in the phase-averaged results of Figure 6 is that the higher-momentum fluid in each jet is concentrated into tubular cores above and below the midspan. There also exists a high-momentum jet along the midspan, which is more aligned along the $y/c = 0$ centerline, for five total jets in the time-averaged wake. These are combined with regions of momentum-deficit (blue) generated immediately behind the trailing edge surrounding the momentum-rich cores.

FIGURE 8

Visualization of the overall wake structure in terms of the time-averaged streamwise velocity for $St = 0.37$. Panels a–d present isosurfaces of $\overline{u}$ that range from 0.8 to 1.40. Panel e shows the distribution of velocity vectors and contours at the plane of the midspan. Panels f–h show the spanwise distribution of $\overline{u}$ at three streamwise locations.

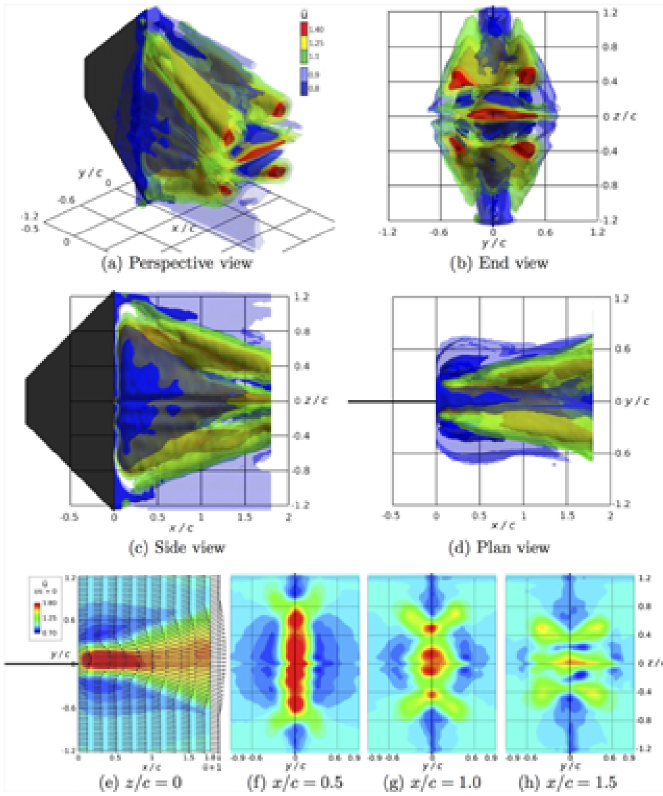

Figures 8e–8h show the time-averaged velocity vectors and streamwise velocity contours in the spanwise symmetry plane, as well as contour plots in streamwise-constant planes at x/c = 0.5, 1.0, and 1.5. As seen in Figure 8(e), the central high momentum jet starts to expand transversely at $x/c \approx 0.7$. The velocity vector profile at the downstream end of the data domain shows that there is a momentum-surplus within $y/c = \pm 0.6$, as indicated by arrows crossing a vertical $\overline{u}$ = 1.0 line. The high-momentum core of the wake at x/c = 0.5 (Figure 8f) is rectangular in section and surrounded by momentum-deficit regions (blue). Farther downstream at x/c = 1 (Figure 8g), there are three concentrated high-momentum regions with lower magnitude streamwise velocity. It is clear that near $z/c = \pm 0.8$, the top and bottom higher-momentum cores are transitioning to the four separate corner cores that are seen at x/c = 1.5 (Figure 8h). During this transition, regions of lower-momentum appear near $z/c = \pm 0.2$, between the central core and the corner cores.

Highest Strouhal Number: St = *0.56*

Four views of time-averaged streamwise velocity ($\overline{u}$) isosurfaces are shown for the highest Strouhal number studied (St = 0.56) in Figure 9. Isosurfaces are included at $\overline{u}$ = 1.1 (green), 1.25 (yellow), and 1.4 (red) to capture the momentum-surplus regions of the wake. Two isosurfaces at $\overline{u}$ = 0.5 and 0.85 (dark blue, light blue) capture the momentum-deficit regions. The overall topology and the behavior patterns of the wake at this St are qualitatively similar to that at St = 0.37. The high-momentum regions exhibit a stronger spanwise compression and here stretch between $z/c = \pm 0.5$ at one chordlength downstream and $z/c = \pm 0.3$ by the downstream edge of the data domain. The time-averaged higher-momentum flow is again organized into four tube-like structures, with two pairs above and below the midspan. Downstream of x/c = 1, the transverse (y) expansion of the jets becomes more exaggerated, and the magnitude of the streamwise velocity decreases, most clearly observed from above in Figure 9d. The central jet that was seen at St = 0.37, however, is not apparent further than one chord length downstream. Similar to the St = 0.37 wake, regions of momentum-deficit flow are shown in blue isosurfaces and again surround the high momentum core along all sides. At this St, a region of low momentum fluid is also apparent across the centerline of the wake downstream of x/c = 1.

Figures 9e–9h show the time-averaged velocity vectors and streamwise velocity contours in the spanwise symmetry plane, as well as contour plots in streamwise-constant planes at x/c = 0.5, 1.0, and 1.5. Contours and velocity vectors on the spanwise symmetry plane show a single jet up to about x/c = 0.8, giving way to two diverging jets with lower streamwise velocity magnitude that are consistent with transverse expansion of the wake. The velocity vectors at the downstream edge of the window indicate two momentum-surplus profiles from $1 < y/c < 0.5$ and $0.6 < y/c < 1.2$, seen in comparisons with the $\overline{u}$ = 1 line. The

FIGURE 9

Visualization of the overall wake structure in terms of the time-averaged streamwise velocity for $St = 0.56$. Panels a–d present isosurfaces of $\overline{u}$ that range from 0.5 to 1.40. Panel e shows the distribution of velocity vectors and contours at the plane of the midspan. Panels f–h show the spanwise distribution of $\overline{u}$ at three streamwise locations.

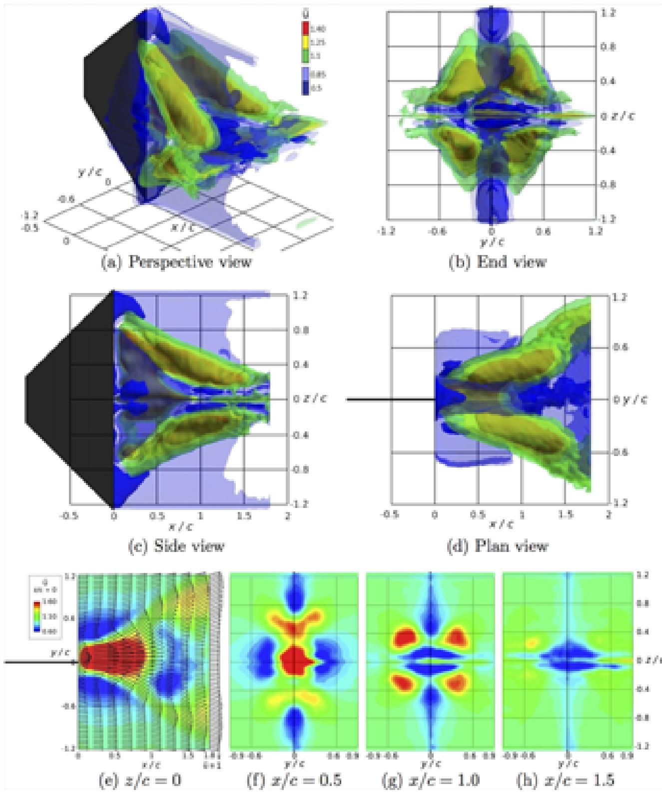

core of the wake at $x/c = 0.5$ (Figure 9f) is similar in shape to the wake of the $St = 0.37$ wake at $x/c = 1$ (Figure 8g), indicating that physical process of wake breakdown may be consistent across Strouhal numbers but moves upstream for increasing St. At $x/c = 1.0$ (Figure 9g), four jets are apparent, but already the loss of the high-momentum core along the centerline is observed. Low-momentum regions are also seen at this downstream location, stretching from $y/c = \pm 0.5$. This is again similar to the shape of the $St = 0.37$ wake further downstream at $x/c = 1.5$ (Figure 8h). Finally, at $x/c = 1.5$ in the $St = 0.56$ wake (Figure 9h), the higher-momentum fluid jets have disintegrated, with a dominant lower-momentum region near the centerline.

Spanwise Variation of Streamwise Momentum Flux

Application of an integral momentum balance in the streamwise direction yields an indirect measurement of thrust or drag based on assumptions that the incoming freestream is uniform, the transverse momentum flux is negligible, and the control volume is far enough from the object so that the local pressure acting on the control surfaces is the undisturbed value of the freestream static pressure. The nondimensional momentum balance equation is given as:

$$T' = \int_{-\infty}^{+\infty} \overline{u}\,(\overline{u} - 1)\,\mathrm{d}\left(\frac{y}{c}\right) \tag{4}$$

where $\overline{u}$ is the time-averaged nondimensional streamwise velocity, c is the chord, and T' is the net time-averaged nondimensional streamwise momentum flux per unit span. T' is proportional to thrust force provided the assumptions listed above are valid. However in practical flows the assumption of uniform freestream pressure on the control surfaces is questionable in the presence of significant spanwise flows (Clark & Smits, 2006; Buchholz & Smits, 2008) and considerable spatial pressure gradients along the panel surface as reported by Green and Smits (2008). In the current study with inadequate streamwise data domain length, Equation 4 cannot yield reliable thrust estimate; however, it can be used to locate the concentration of thrust-generating momentum flux along the span.

Figure 10 shows T' for all five Strouhal numbers at three downstream locations of $x/c = 0.5$, 1.0, and 1.5. Only the upper half of the span has been represented, assuming spanwise symmetry. At all three x/c locations, the tip region of the panel ($z/c > 1$) shows a net deficit in streamwise momentum flux per unit span T'. This is also supported by the isosurfaces of time-averaged streamwise velocity (Figures 7, 8, and 9), where this region is dominated by streamwise momentum-deficit isosurfaces.

Further toward the midspan, the momentum fluxes peak once before maximizing again at the midspan for $St \geq 0.37$. The peaks away from the midspan correspond to the increased momentum jets induced by the wake structures, which are angled downward from the panel tips at the higher St. This 3D effect induced by the tip vortices induces spanwise flows that transport momentum from the tip toward the midspan of the fin while convecting downstream and has been observed before by Clark and Smits

FIGURE 10

Spanwise variation of net nondimensional streamwise momentum flux per unit span at different downstream locations.

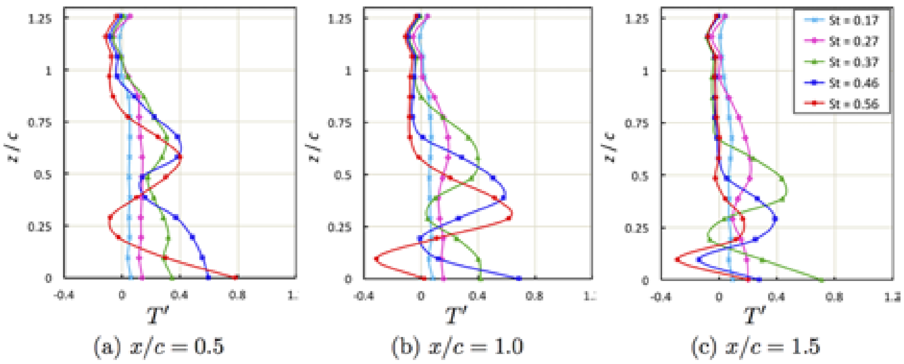

(2006) and Buchholz and Smits (2008). These jets were observed for all but the lowest Strouhal number case, where the momentum flux per unit span remains approximately constant along the span. The momentum flux attains a maximum again at the midspan, which is expected as flow in the midspan region is close to 2D.

At a location one-half chord length downstream, the higher Strouhal number flows at St = 0.37, 0.46, and 0.56 have a time-averaged streamwise momentum peak near $z/c \approx 0.68$, 0.63, and 0.58, respectively. The off-midspan peaks move inboard at the two downstream locations, appearing near $z/c \approx 0.58$, 0.4, and 0.33 for St = 0.37, 0.46, and 0.56, respectively, at one chord length downstream, and $z/c \approx 0.45$, 0.3, and 0.25 at x/c = 1.5. Interestingly, while there is only the one peak at the midspan for St = 0.27 at x/c = 0.5, small peaks appear near $z/c \approx 0.62$, and 0.52 at x/c = 1.0 and 1.5, respectively.

Transverse Wake Bifurcation

As shown in Figures 8 and 9, high-momentum fluid is broken into multiple transverse jets as Strouhal number increases. This is caused by strong vortex loop interaction and greater-magnitude vortex-induced velocities in the transverse as well as spanwise directions, resulting in the bifurcated jets, which diverge in the transverse plane and converge in the spanwise plane (Buchholz & Smits 2006).

Time-averaged velocity field contours in a plane at z/c = 0.64, which lies one quarter span above the plane of symmetry, are presented in Figure 11 for the five Strouhal numbers. Results are shown in this plane, because in the St = 0.37 and St = 0.56 cases additional high-momentum fluid is observed at the midspan, which complicates diagnosis of the jet structures away from the midspan. A single coherent jet structure throughout the length of domain at St = 0.17 (Figure 11a) indicates that the wake bifurcation does not occur within the observation window. At St = 0.27 (Figure 11b), the wake bifurcates at $x/c \approx 1.5$. The bifurcation point moves upstream, and the angle that the bifurcated jets make with the streamwise direction (θ_{bi}) becomes steeper with increasing St (Figures 11b–11e). Similar observations were made for a heaving and pitching foil with elliptic planform by Dong et al. (2006), for a rigid pitching panel by Buchholz and Smits (2006), and for an oscillating batoid-inspired flexible fin with elliptic planform by Dewey et al. (2012).

The bifurcation distance (X_{bi}) and the bifurcation angle (θ_{bi}) were estimated by drawing a trendline through the local maxima of the $(u - U)/U$ profile (von Ellenrieder & Pothos, 2008)

FIGURE 11

Time-averaged velocity fields at the quarter span for all five Strouhal numbers (panel shown as broken line to indicate that it is not drawn to scale).

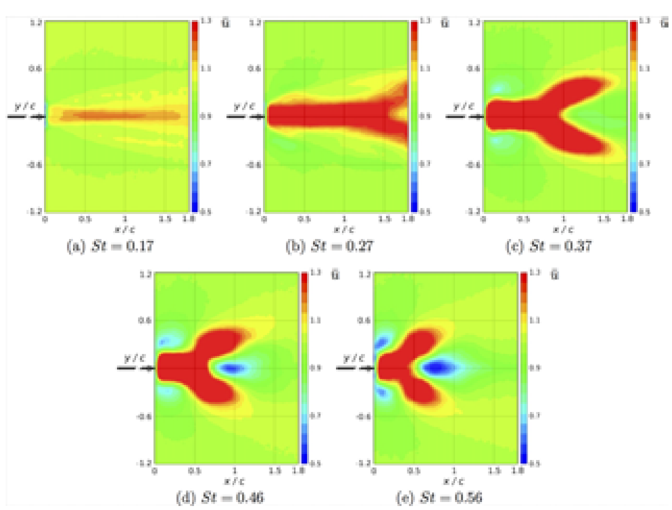

at a minimum of three *x/c* locations immediately downstream of the qualitatively observed bifurcation. The bifurcation distances and angles measured in this way are shown as a function of *St* in Figure 12. Bifurcation distance decreases and the bifurcation angle increases with increase in Strouhal number. This is expected as wake bifurcation occurs when the vortex loops generated by the oscillating panel are strong enough to self-induce themselves away from the line of symmetry (Buchholz & Smits, 2006; Dong et al., 2006). In the current work, vortex strength increases with increasing *St*, seen by comparing the spanwise vortices in Figures 4d, 5d, and 6d, where the size of the vortices, represented by the same contour levels, increases with *St*. Also with the increasing *St*, the transverse splitting occurs at a shorter distance downstream of the trailing edge as seen in Figures 11 and 12. Results from the current study exhibit similar trends to the results on an oscillating batoid-inspired flexible fin with elliptic planform by Dewey et al. (2012). The bifurcation distance, X_{bi}, however, drops faster with increasing *St* in the present study, possibly due to difference in the planform shapes. The bifurcation angle in this study tends toward ≈27°, close to the value of ≈25° observed by Dewey et al. (2012).

Discussion

Insight into the hydrodynamics and the evolution of the wake downstream of a trapezoidal pitching panel, chosen as a model of fish caudal fins, has been gained by the analysis of the 3D velocity fields. The wake downstream of the panel was captured using stereoscopic PIV, and both phase-averaged velocity as well as time-averaged velocity fields were studied. The 3D wakes behind finite *AR* oscillating panels and fins behave significantly differently compared to 2D wakes. 3D effects enter the wake through the streamwise vortices at the spanwise edges of the wake. These streamwise vortices generate transverse and spanwise flows that cause bending of the interconnected vortex loops that comprise the wake, consequently causing spanwise compression and transverse expansion wake structures.

The vortex loop structures induce flow that adds downstream momentum, indicative of thrust production by the panel motion. This is a pattern that has also been observed behind pectoral fins of bluegill sunfish by Drucker and Lauder (1999). The nondimensional momentum of the induced flow relative to the freestream increases with increasing Strouhal number, as indicated by the rising isosurface levels of the phase-averaged velocity that enclose approximately the same area and have the same spatial structure at higher *St*. With increasing *St* comes increasing wake complexity, however, and at the higher *St*, regions with streamwise velocity less than the freestream also appear surrounding the high-momentum cores. These lower-momentum regions also increase in size and decrease in velocity magnitude as *St* increases, which could be related to the decrease in efficiency at higher *St* that has been repeatedly observed in the literature.

Another consequence of 3D effects is the splitting of the two sets of interconnected vortex loops. These sets of vortex loops on either side of the transverse (y) plane of symmetry induce flow through their centers, and at higher *St* divide the central momentum-rich core of the wake into two thrust-producing jets, similar to those observed by Dong et al. (2006); Buchholz and Smits (2006); Dewey et al. (2012). These wake structures are further divided above and below the spanwise (z) symmetry plane, resulting in four jets that diverge in the transverse direction and converge in spanwise direction. In addition to these four jets, there is a central momentum-rich jet associated with quasi-2D flow in the vicinity of $z/c = 0$ plane. This is similar to an observation made by Dong et al. (2006) for a panel with elliptic planform and $AR = 5.09$, where four jets clearly appear as a four-lobed structure in the streamwise planes. In this study, however, this central momentum-rich jet disappears downstream of $x/c = 1$ at

FIGURE 12

Transverse bifurcation distance and angle as a function of Strouhal number.

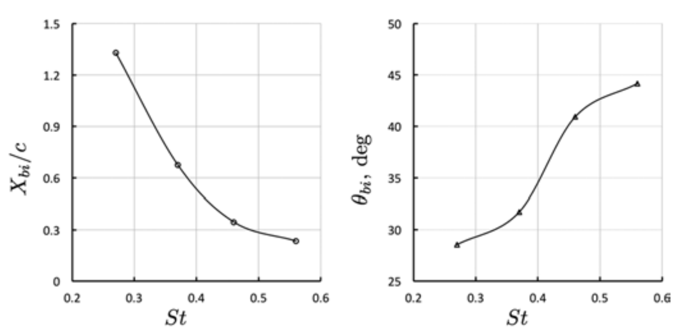

(a) Transverse bifurcation distance (b) Transverse bifuration angle

St = 0.56. The convergence of jets in the spanwise direction is also indicated by the spanwise shift of the peak of nondimensional streamwise momentum flux per unit span from a region close to tips toward the midspan as we move downstream from the trailing edge (Figure 10).

These observations of the changing wake structure, especially in terms of the spatial distribution and magnitude of the streamwise momentum, are by and large consistent with most of the literature concerning how averaged thrust and efficiency behave with Strouhal number for low *AR* fin models. Generally, the coefficient of thrust increases with increasing St but efficiency peaks at an intermediate St before decreasing. In the current results, we show that, within the shed vortex loops, the magnitude of nondimensional streamwise velocity relative to the freestream increases with increasing St both in the phase-averaged and time-averaged results. However, as St increases, regions of sluggish low-momentum fluid also become apparent in the internal wake structure. This possibly explains the decrease in efficiency that accompanies the increase in coefficient of thrust at higher St, often seen in the literature. Appearance of these low streamwise momentum pockets between the diverging thrust-producing jets is due to an increasingly larger proportion of incoming momentum flux being diverted in the transverse direction through the interconnected diverging loops at higher St, leaving a deficit in streamwise momentum flux that manifests as sluggish flow pockets (Buchholz & Smits, 2006; Dong et al., 2006; Clark & Smits, 2006; Dewey et al., 2012).

The increasingly larger proportion of incoming momentum flux that is redirected away from the wake midline as St increases is also consistent with the transverse wake bifurcation. The vortices generated at the panel edges have an increased magnitude with increasing St and shed more frequently, causing stronger vortex interaction and larger magnitude vortex-induced transverse velocities, which essentially push alternating vortex loops away from the midline and create the bifurcated wake structure. The downstream distance at which this bifurcation occurs decreases, and the angle that the bifurcated jets make with the streamwise direction increases, with increasing St. The variation of the bifurcation distance with St and bifurcation angle for the trapezoidal panel exhibits trends similar to those obtained by Dewey et al. (2012) on a batoid-inspired flexible fin with elliptic planform in undulatory oscillations. The decrease in bifurcation distance with increase in St, however, is steeper for the trapezoidal panel in the present study. It is also important to note that the jet bifurcation described here is consistent with the wake breakdown observed and described by Green et al. (2011). That previous work did not investigate the spatial distribution of the streamwise velocity, focusing instead on the evolution of the vorticity. The bifurcation of the jets and the disintegration of the individual coherent spanwise vortices appear to be the same phenomenon, apparent in Figures 5d and 6d.

The current results provide a sense of the spatial and temporal structure of the stream-wise momentum, which will potentially lead to improved geometry and actuation design strategies for preserving the creation of high-momentum flow regions while mitigating the creation of the low-momentum regions.

Acknowledgments

This work was supported by the Office of Naval Research under ONR Award No. N00014-14-1-0418.

Corresponding Author:

Rajeev Kumar
Department of Mechanical and Aerospace Engineering, Syracuse University
263 Link Hall, Syracuse, NY 13244
Email: rkuma103@syr.edu

References

Anderson, J.M., Streitlein, K., Barrett, D.S., & Triantafyllou, M.S. 1998. Oscillating foils of high propulsive efficiency. J Fluid Mech. 360:41-72. http://dx.doi.org/10.1017/S0022112097008392.

Blondeaux, P., Fornarelli, F., Guglielmini, L., Triantafyllou, M.S., & Verzicco, R. 2005. Numerical experiments on flapping foils mimicking fish-like locomotion. Phys Fluids. 17:113601. http://dx.doi.org/10.1063/1.2131923.

Buchholz, J.H.J., Green, M.A., & Smits, A.J. 2011. Scaling the circulation shed by a pitching panel. J Fluid Mech. 688:591-601. http://dx.doi.org/10.1017/jfm.2011.408.

Buchholz, J.H.J., & Smits, A.J. 2006. On the evolution of wake structure produced by a low-aspect-ratio pitching panel. J Fluid Mech. 546:433-43. http://dx.doi.org/10.1017/S0022112005006865.

Buchholz, J.H.J., & Smits, A.J. 2008. The wake structure and thrust performance of a rigid low-aspect-ratio pitching panel. J Fluid Mech. 603:331-65. http://dx.doi.org/10.1017/S0022112008000906.

Clark, R.P., & Smits, A.J. 2006. Thrust production and wake structure of a batoid-inspired oscillating fin. J Fluid Mech. 562:415-29. http://dx.doi.org/10.1017/S0022112006001297.

Dabiri, J.O. 2005. On the estimation of swimming and flying forces from wake measurements. J Exp Biol. 208:3519-32. http://dx.doi.org/10.1242/jeb.01813.

Dewey, P.A., Carriou, A., & Smits, A.J. 2012. On the relationship between efficiency and wake structures of a batoid-inspired oscillating fin. J Fluid Mech. 691:245-66. http://dx.doi.org/10.1017/jfm.2011.472.

Dong, H., Mittal, R., & Najjar, F.M. 2006. Wake topology and hydrodynamic performance of low-aspect-ratio flapping foils. J Fluid Mech. 566:309-43. http://dx.doi.org/10.1017/S002211200600190X.

Drucker, E., & Lauder, G.V. 1999. Locomotor forces on a swimming fish: Three dimensional vortex wake dynamics quantified using digital particle image velocimetry. J Exp Biol. 202:2393-412.

Drucker, E., & Lauder, G.V. 2002. Experimental hydrodynamics of fish locomotion: functional insights from wake visualization. Integr Comp Biol. 42:243-57. http://dx.doi.org/10.1093/icb/42.2.243.

von Ellenrieder, K.D., Parker, K., & Soria, J. 2003. Flow structures behind a heaving and pitching finite-span wing. J Fluid Mech. 490:129-38. http://dx.doi.org/10.1017/S0022112003005408.

von Ellenrieder, K.D., & Pothos, S. 2008. PIV measurement of the asymmetric wake of a two-dimensional heaving hydrofoil. Exp Fluids. 44:733-45. http://dx.doi.org/10.1007/s00348-007-0430-z.

Epps, B.P., & Techet, A.H. 2007. Impulse generated during unsteady maneuvering of swimming fish. Exp Fluids. 43:691-700. http://dx.doi.org/10.1007/s00348-007-0401-4.

Ghovardhan, R., & Williamson, C.H.K. 2005. Vortex-induced vibrations of a sphere. J Fluid Mech. 531:11-47. http://dx.doi.org/10.1017/S0022112005003757.

Godoy-Diana, R., Aider, J., & Wesfreid, J.E. 2008. Transition in the wake of a flapping foil. Phys Rev E. 77:016308. http://dx.doi.org/10.1103/PhysRevE.77.016308.

Green, M.A., Rowley, C.W., & Smits, A.J. 2011. The unsteady three-dimensional wake produced by a trapezoidal pitching panel. J Fluid Mech. 685:117-45. http://dx.doi.org/10.1017/jfm.2011.286.

Green, M.A., & Smits, A.J. 2008. Effects of three-dimensionality on thrust production by a pitching panel. J Fluid Mech. 615:211-20. http://dx.doi.org/10.1017/S0022112008003583.

Guglielmini, L. 2004. Modeling of thrust generating foils. PhD thesis, University of Genoa.

Guglielmini, L., & Blondeaux, P. 2004. Propulsive efficiency of oscillating foils. Eur J Mech B-Fluid. 23:255-78. http://dx.doi.org/10.1016/j.euromechflu.2003.10.002.

Hultmark, M., Leftwich, M., & Smits, A.J. 2007. Flowfield measurements in the wake of a robotic lamprey. Exp Fluids. 43:683-90. http://dx.doi.org/10.1007/s00348-007-0412-1.

Hunt, J.C.R., Wray, A.A., & Moin, P. 1988. Eddies, streams, and convergence zones in turbulent flows. Proceedings of Summer Program, pp. 193-208. Moffett Field, CA: NASA, Ames Research Center.

Koochesfahani, M.M. 1989. Vortical patterns in the wake of an oscillating foil. AIAA J. 27(9):1200-05. http://dx.doi.org/10.2514/3.10246.

Lawson, N.J., & Wu, J. 1997. Three-dimensional particle image velocimetry: error analysis of stereoscopic techniques. Meas Sci Technol. 8:894-900. http://dx.doi.org/10.1088/0957-0233/8/8/010.

Martínez-Suástegui, L. 2012. Overview on Stereoscopic Particle Image Velocimetry, Advanced Methods for Practical Applications in Fluid Mechanics. Prof. Jones, Steven (Ed.), ISBN: 978-953-51-0241-0, InTech, Rijeka, Croatia.

Parker, K., von Ellenrieder, K.D., & Soria, J. 2005. Using stereo multigrid DPIV (SMDPIV) measurements to investigate the vortical skeleton behind a finite-span flapping wing. Exp Fluids. 39:281-98. http://dx.doi.org/10.1007/s00348-005-0971-y.

Parker, K., von Ellenrieder, K.D., & Soria, J. 2007a. Morphology of the forced oscillatory flow past a finite-span wing at low Reynolds number. J Fluid Mech. 571:327-51. http://dx.doi.org/10.1017/S0022112006003491.

Parker, K., von Ellenrieder, K.D., & Soria, J. 2007b. Thrust measurements from a finite-span flapping wing. AIAA J. 45:58-70. http://dx.doi.org/10.2514/1.18217.

Prasad, A.K., & Jensen, K. 1995. Scheimpflug stereocamera for particle image velocimetry in liquid flows. Appl Optics. 34(30):7092-9. http://dx.doi.org/10.1364/AO.34.007092.

Raffel, M., Willert, C.E., Wereley, S.T., & Kompenhans, J. 2007. Particle Image Velocimetry: A Practical Guide. NY: Springer.

Triantafyllou, G.S., Triantafyllou, M.S., & Grosenbaugh, M.A. 1993. Optimal thrust development in oscillating foils with application to fish propulsion. J Fluid Struct. 7:205-24. http://dx.doi.org/10.1006/jfls.1993.1012.

Triantafyllou, M.S., Triantafyllou, G.S., & Yue, D. 2000. Hydrodynamics of fishlike swimming. Annu Rev Fluid Mech. 32(1): 33-53. http://dx.doi.org/10.1146/annurev.fluid.32.1.33.

Williamson, C.H.K., & Roshko, A. 1988. Vortex formation in the wake of an oscillating cylinder. J Fluid Struct. 2:355-81. http://dx.doi.org/10.1016/S0889-9746(88)90058-8.

Yu, M.L., Hu, H., & Wang, Z.J. 2012, January. Experimental and numerical investigations on the asymmetric wake vortex structures around an oscillating airfoil. In 50th AIAA Aerospace Sciences. Meeting including the New Horizons Forum and Aerospace Exposition, AIAA Paper (Vol. 299).

Zhu, Q., & Shoele, K. 2008. Propulsion performance of a skeleton-strengthened fin. J Exp Biol. 211:2087-100. http://dx.doi.org/10.1242/jeb.016279.